nature communications

Article

https://doi.org/10.1038/s41467-025-59472-0

Engineering high-density microcrystalline boundary with V-doped RuO_2 for high-performance oxygen evolution in acid

Received: 25 June 2024

Accepted: 22 April 2025

Published online: 14 May 2025

Check for updates

Han Wu[1,6], Zhanzhao Fu[2,6], Jiangwei Chang[1] ✉, Zhiang Hu[1], Jian Li[1], Siyang Wang[1], Jingkun Yu[1], Xue Yong[3], Geoffrey I. N. Waterhouse[4], Zhiyong Tang[5], Junbiao Chang[1] & Siyu Lu[1] ✉

Designing efficient acidic oxygen evolution catalysts for proton exchange membrane water electrolyzers is challenging due to a trade-off between activity and stability. In this work, we construct high-density microcrystalline grain boundaries (GBs) with V-dopant in RuO_2 matrix (GB-V-RuO_2). Our theoretical and experimental results indicate this is a highly active and acid-resistant OER catalyst. Specifically, the GB-V-RuO_2 requires low overpotentials of 159, 222, and 300 mV to reach 10, 100, and 1500 mA cm^{-2}_{geo} in 0.5 M H_2SO_4, respectively. Operando EIS, ATR-SEIRAS FTIR and DEMS measurements reveal the importance of GBs in stabilizing lattice oxygen and thus inhibiting the lattice oxygen mediated OER pathway. As a result, the adsorbate evolution mechanism pathway becomes dominant, even at high current densities. Density functional theory analyses confirm that GBs can stabilize V dopant and that the synergy between them modulates the electronic structure of RuO_2, thus optimizing the adsorption of OER intermediate species and enhancing electrocatalyst stability. Our work demonstrates a rational strategy for overcoming the traditional activity/stability dilemma, offering good prospects of developing high-performance acidic OER catalysts.

The electrolysis of water is considered the most promising method for producing hydrogen and achieving carbon neutrality in the energy sector[1,2]. Proton exchange membrane water electrolyzers (PEMWEs) have attracted widespread attention because of their many advantages including high-purity hydrogen, fast system response, and large operating current[3,4]. However, the rapid performance degradation of anode catalysts due to corrosion in harsh acidic environments greatly hinders their commercial application[5]. Developing efficient and highly acid-stable ruthenium/iridium (Ru/Ir) -based catalysts for anodic oxygen evolution reaction (OER) in acidic media has become a research imperative[6–8]. Compared with IrO_2, rutile-structured RuO_2 has a higher OER activity and lower price, but its stability is generally much lower[9]. Vojvodic et al. found that coordinatively-unsaturated Ru sites on RuO_2 (110) surfaces are soluble during OER[10], leading to catalyst corrosion. Alexandrov et al. demonstrated that during the OER process, the dissolution of RuO_2 produces soluble high valence Ru species ($Ru^{\delta+}$, $\delta > 4$), including $RuO_2(OH)$ and $RuO_2(OH)_2$[11]. These metastable species are beneficial for achieving high OER activity, but destroy the parent RuO_2 structure, resulting in poor stability (hence the root cause of high activity and instability are the same). Most strategies developed to date in an attempt to mitigate Ru dissolution are inadequate, especially when PEMWEs are operated at high current densities[12,13].

[1]College of Chemistry and Pingyuan Laboratory, Zhengzhou University, Zhengzhou 450001, P.R. China. [2]State Key Laboratory for Clean Energy Utilization, Institute for Thermal Power Engineering, Zhejiang University, Hangzhou 310027, P.R. China. [3]Department of Electrical Engineering and Electronics, University of Liverpool, Liverpool L69 3GJ, UK. [4]School of Chemical Sciences, The University of Auckland, Auckland 1142, New Zealand. [5]CAS Key Laboratory of Nanosystem and Hierarchical Fabrication, CAS Center for Excellence in Nanoscience, National Center for Nanoscience and Technology, Beijing, P.R. China. [6]These authors contributed equally: Han Wu, Zhanzhao Fu. ✉e-mail: jwchang2021@zzu.edu.cn; sylu2013@zzu.edu.cn

The adsorption evolution mechanism (AEM) has been widely reported on RuO_2 in the OER process, where a high theoretical overpotential of 0.37 V was required owing to the linear scaling relationship between O-containing intermediates[14]. The localized structure of Ru−O bonds can significantly affect the OER activity of RuO_2-based electrocatalysts. Effective strategies, including defect engineering[15–17], element doping[18–20], interface engineering[21,22], and strain engineering[23,24], have been developed to fabricate Ru-based catalysts with modified Ru −O localized structures. Previous studies have revealed that strengthening the Ru−O bond covalency can effectively enhance the catalytic activity of RuO_2 via enabling lattice oxygen mediated oxygen evolution mechanism (LOM), thus breaking the thermodynamic limitations of the AEM pathway[25,26]. In the LOM pathway, the OER process is triggered via electrochemical activation of lattice O, where a high orbital overlap between O 2*p* and Ru 3*d* can be found, and simultaneously avoids the generation of OOH intermediates, thus breaking the linear scaling relationship commonly encountered for AEM[27,28]. However, fast OER kinetics via the LOM pathway is usually accompanied by a deterioration in electrocatalyst stability, in which highly oxidized Ru species, O vacancy-induced phase reconstruction and structural collapse occur, greatly reducing the lifetime of the catalyst[29,30]. To achieve a better activity-stability balance in RuO_2, Ge et al. introduced guest elements to regulate the local structure of Ru −O, where the OER path of the catalyst can be tuned between AEM and LOM by selecting specific doped metals with different ionic electronegativity[31]. Recently, our group reported that introducing zinc atoms into the RuO_2 matrix can effectively regulate the electronic structure of active Ru atoms, thus optimizing the binding strength of O adsorbates during OER and greatly improving both the activity and stability of RuO_2[32]. Although element doping can significantly enhance the OER activity of RuO_2 via directly adjusting the Ru−O localized structures, the OER performance of the catalyst highly depends on the guest atoms. Often, the doped bulk phases become unstable and corrode, leading to unsatisfactory OER performance under high current conditions. Therefore, effective strategies need to be developed adopting an integrated design of Ru−O coordination and phase structures for improving the activity and stability of RuO_2 simultaneously.

Herein, we report a fast thermal-driven cation exchange strategy to introduce a high density of sufficient microcrystalline grain boundaries (GBs) into a V-doped RuO_2 matrix without any templating agents. The presence of a high-density of GBs in the GB-V-RuO_2 catalyst was verified using X-ray absorption spectroscopy (XAS), X-ray photoelectron spectroscopy (XPS) and aberration-corrected scanning transmission electron microscopy (AC-STEM). At the atomic level, we demonstrate that the introduction of atomic V and GBs precisely regulated the local Ru−O bonding, resulting in more low-valent and low-coordination Ru sites and a weakened Ru−O hybridization. Consequently, the GB-V-RuO_2 catalyst delivered both good activity and stability for catalyzing OER in acidic media. Specifically, low overpotentials of 159 and 300 mV were required to reach 10 and 1500 mA cm^{-2}_{geo}, respectively. Furthermore, the electrocatalyst operated stably with long lifetimes of 760 h at 10 mA cm^{-2}_{geo} for acidic OER, far exceeding commercial RuO_2 and IrO_2 (Com. RuO_2/Com. IrO_2). Operando differential electrochemical mass spectroscopy (DEMS) and attenuated total refraction surface-enhanced infrared spectroscopy (ATR-SEIRAS IR) studies revealed that the introduction of GBs significantly inhibits the LOM pathway via stabilizing lattice O, with an AEM-dominant OER pathway still be retained over the entire OER window, thus ensuring the efficient and stable OER process under high current densities. Density functional theory (DFT) analyses further confirm that V doping and GBs can effectively modify the electronic structure of RuO_2, thus optimizing the adsorption of oxygen intermediates and providing a lower energy OER route.

Results

Electrocatalyst characterization

The catalysts were prepared using a rapid thermal-driven cation exchange strategy (Fig. 1a, See details in Materials and Methods, Supplementary Note 1 and Supplementary Fig. 1), where the crystallization process and GB density in the catalysts were precisely regulated via directly controlling the reaction temperature. We found that the RuO_2 product obtained at low temperatures (~350 °C) had smaller crystalline domains with high-density GBs (GB-V-RuO_2) (Supplementary Figs. 2 and 3), whereas the RuO_2 single crystals (V-RuO_2) can be obtained at high temperatures (~700 °C). As shown in Fig. 1b, the powder X-ray diffraction (XRD) patterns of GB-V-RuO_2 and V-RuO_2 both matched that of the rutile RuO_2 phase (JCPDS no. 43-1027) with no obvious impurities. It should be also noted that the diffraction peaks of GB-V-RuO_2 had a larger full width at half-maximum, implying a smaller crystalline domain size. Aberration-corrected high-angle annular dark-field scanning transmission electron microscopy (AC-HAADF STEM, Fig. 1c and Supplementary Fig. 4) revealed that GB-V-RuO_2 comprised small crystalline domains (size of ~6.37 nm). Note that it doesn't affect the generation of grain boundaries with or without the introduction of V (Supplementary Fig. 5). Moreover, GBs were well-distributed in the bulk phase of GB-V-RuO_2 (the white dashed lines represent GBs). The magnified HAADF-STEM image (Fig. 1d-f) of GB-V-RuO_2 revealed the multiple exposed crystal faces of a rutile RuO_2 phase, where the lattice fringe spacings of 2.43 and 3.27 Å could readily be assigned to the (101) and (110) facets of RuO_2, respectively[33]. Meanwhile, V atoms were located at Ru atom positions. The corresponding fast Fourier transform pattern (inset of Fig. 1d) confirmed the polycrystal nature of GB-V-RuO_2. In contrast, V-RuO_2 exhibited single crystalline characteristics (no GBs) and a homogeneous distribution of V atoms (Fig. 1g and h, Supplementary Figs. 6 and 7). Differences in crystal structure between GB-V-RuO_2 and V-RuO_2 were also verified using the Raman spectroscopy (Supplementary Fig. 8). As shown in Fig. 1i-l, the local crystal structures of GBs and twin boundaries in GB-V-RuO_2 were next studied using high-resolution HAADF-STEM imaging. Energy-dispersive X-ray spectroscopy (EDX, Fig. 1m and n) elemental mapping profiles of GB-V-RuO_2 further showed a uniform distribution of V, Ru and O within RuO_2 matrix without obvious Ru and V aggregation. The V content of GB-V-RuO_2 was determined to be 3.75 wt%, which was similar to that of V-RuO_2. Also, inductively-coupled plasma optical emission spectroscopy (ICP-OES) analysis of GB-V-RuO_2 indicated that approximately 4.36 wt% V was successfully implanted into the RuO_2 matrix (Supplementary Table 1), indicative of an abundance of asymmetric Ru−O − V structural motifs. The Ru−O − V structure motifs and GBs in GB-V-RuO_2 were expected to significantly change the local electronic structure of Ru−O sites, thus greatly affecting the OER behavior of RuO_2.

We first performed X-ray photoelectron spectroscopy (XPS) analysis to clarify the electronic structure of GB-V-RuO_2 with a Com. RuO_2 powder as a reference. The survey XPS spectrum for GB-V-RuO_2 (Supplementary Figs. 9 and 10) confirmed that the V atoms were successfully introduced. The core-level $V_{3/2}$ 2*p* spectrum (Fig. 2a) showed two peaks at 515.3 and 516.9 eV, which could readily be ascribed to V^{4+} and V^{5+} species, respectively. No peaks due to V^0 species were found. As shown in Fig. 2b, the core-level Ru 3*p* spectrum for GB-V-RuO_2 showed two sets of peaks, each in a 2:1 area ratio, indicating mixed oxidation states of Ru^{3+} and Ru^{4+}. Compared with Com. RuO_2, GB-V-RuO_2 exhibited a lower average oxidation state of Ru atoms (the Ru^{3+} / Ru^{4+} ratio for GB-V-RuO_2 was 0.48, compared to 0.39 for Com. RuO_2). Differences in electronic structures of GB-V-RuO_2 and Com. RuO_2 were further confirmed by examining the core-level O 1*s* spectra (Fig. 2c), where a lower lattice O concentration was observed for GB-V-RuO_2. Since the Ru-O coordination environment determines the electronic structure and OER activity/stability of RuO_2-based electrocatalysts, we used X-ray absorption spectroscopy (XAS) to further study the

modified electronic structure of the GB-V-RuO_2 catalyst. Ru K-edge X-ray absorption near-edge structure (XANES) spectra for the GB-V-RuO_2 catalyst along with reference data for Com. RuO_2 and Ru foil are shown in Fig. 2d. The absorption edge position for the GB-V-RuO_2 was located between those of Com. RuO_2 and Ru foil, indicating a lower oxidation state than Com. RuO_2, in agreement with the results of XPS analysis. The Ru K-edge extended X-ray absorption fine structure (EXAFS, Fig. 2e) spectrum of GB-V-RuO_2 catalyst showed two main peaks in R space at 1.46 and 3.01 Å, corresponding to Ru−O and Ru−O−Ru scattering paths, respectively. Notably, the intensity of Ru−O−Ru (second shell) scattering path for GB-V-RuO_2 catalyst was obviously weaker than that of Com. RuO_2, implying the unsaturated coordination structure due to the presence of asymmetrical Ru−O − V structure motifs and abundant GBs in GB-V-RuO_2[34], which was also confirmed by the corresponding Ru k^3-weighted wavelet transform (WT)-EXAFS spectra (Supplementary Fig. 11). Soft X-ray O K-edge XAS tests were also carried out to obtain deeper insights into the electronic structure modulation in the GB-V-RuO_2 catalyst (Fig. 2f). Two pre-edge peaks at ~529 and ~531 eV were observed for both GB-V-RuO_2 and Com. RuO_2, representing t_{2g} and e_g orbitals hybridization with unoccupied O 2p orbitals, respectively[35,36]. GB-V-RuO_2 had a smaller t_{2g}/e_g intensity ratio of 1.10 compared with Com. RuO_2 (1.20), suggesting a lower degree of hybridization and more unoccupied Ru states for GB-V-RuO_2[37]. Considering that the valence orbitals of metal atoms are directly bound to O-containing intermediates during OER, the binding strength of oxygen intermediates during OER process will be affected due to the difference in the unoccupied orbital states of e_g and t_{2g}. Figure 2g showed the V K-edge XANES spectra of GB-V-RuO_2, Com. VO_2 and V foil. The absorption edge of GB-V-RuO_2 was close to that of Com. VO_2, indicating an average V valence state of ~4. The corresponding V K-edge

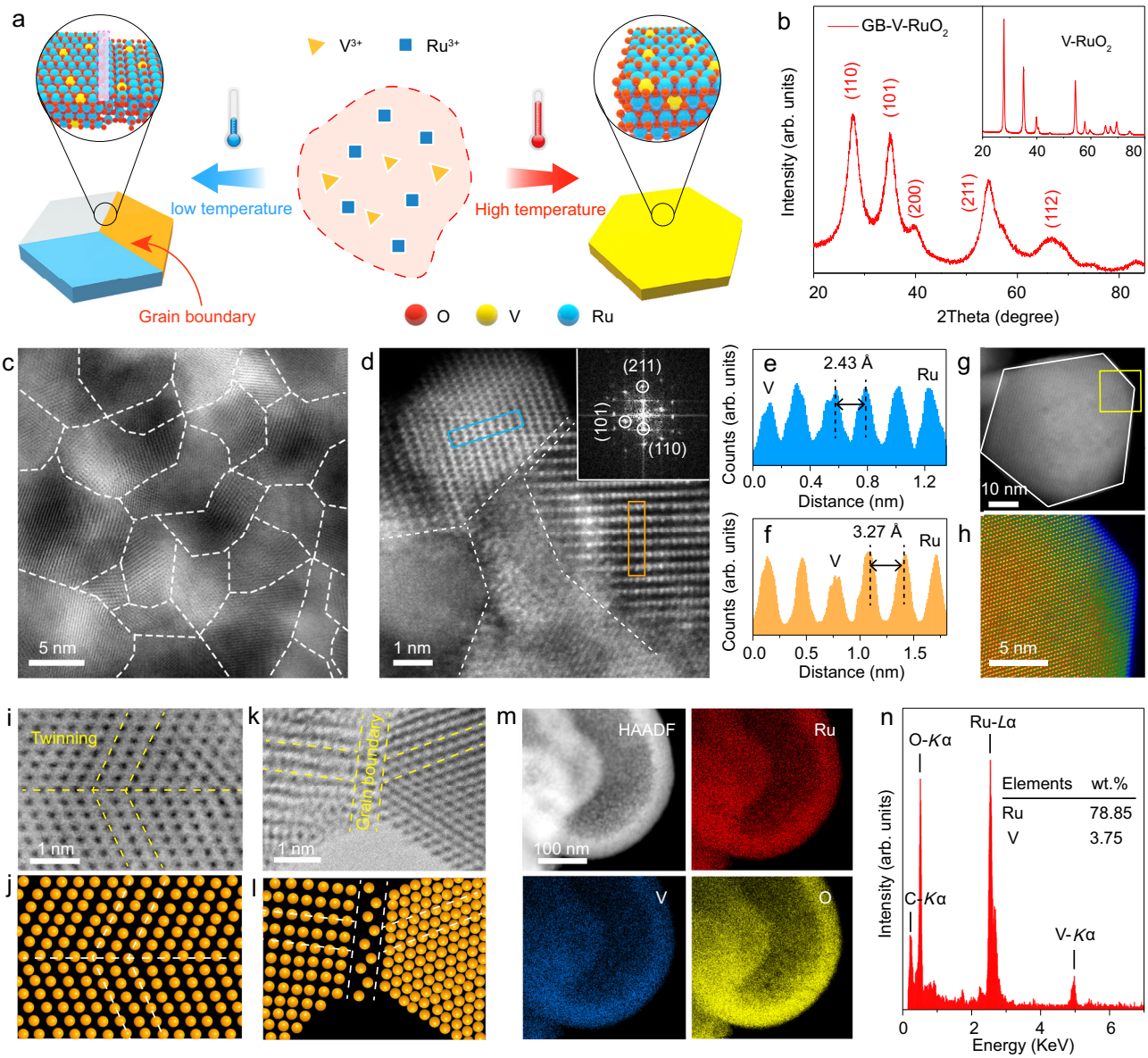

Fig. 1 | Synthesis route and catalyst characterization. a Diagram of the synthesis procedure for GB-V-RuO_2 (left) and V-RuO_2 (right). **b** XRD patterns of GB-V-RuO_2 and V-RuO_2. **c** Aberration-corrected HAADF-STEM image of GB-V-RuO_2, with the abundant grain boundaries marked with white dashed lines. **d** Magnified HAADF-STEM image of GB-V-RuO_2. Inset shows the corresponding fast Fourier transform pattern. **e**, **f** are the intensity profiles of the blue and orange boxes in (**d**), respectively. **g** HAADF-STEM image of V-RuO_2. **h** shows the temperature-scale image of the selected region in (**g**). **i** and **k** show the presence of twinning and a GB in GB-V-RuO_2, respectively. **j** and **l** illustrate the atomic arrangement of twinning and a GB, respectively. **m**, **n** HAADF-STEM together with elemental mappings of Ru, V and O atoms in GB-V-RuO_2, and corresponding EDX spectrum. Scale bar, 100 nm. Source data for Fig. 1 are provided as a Source Data file.

https://doi.org/10.1038/s41467-025-59472-0

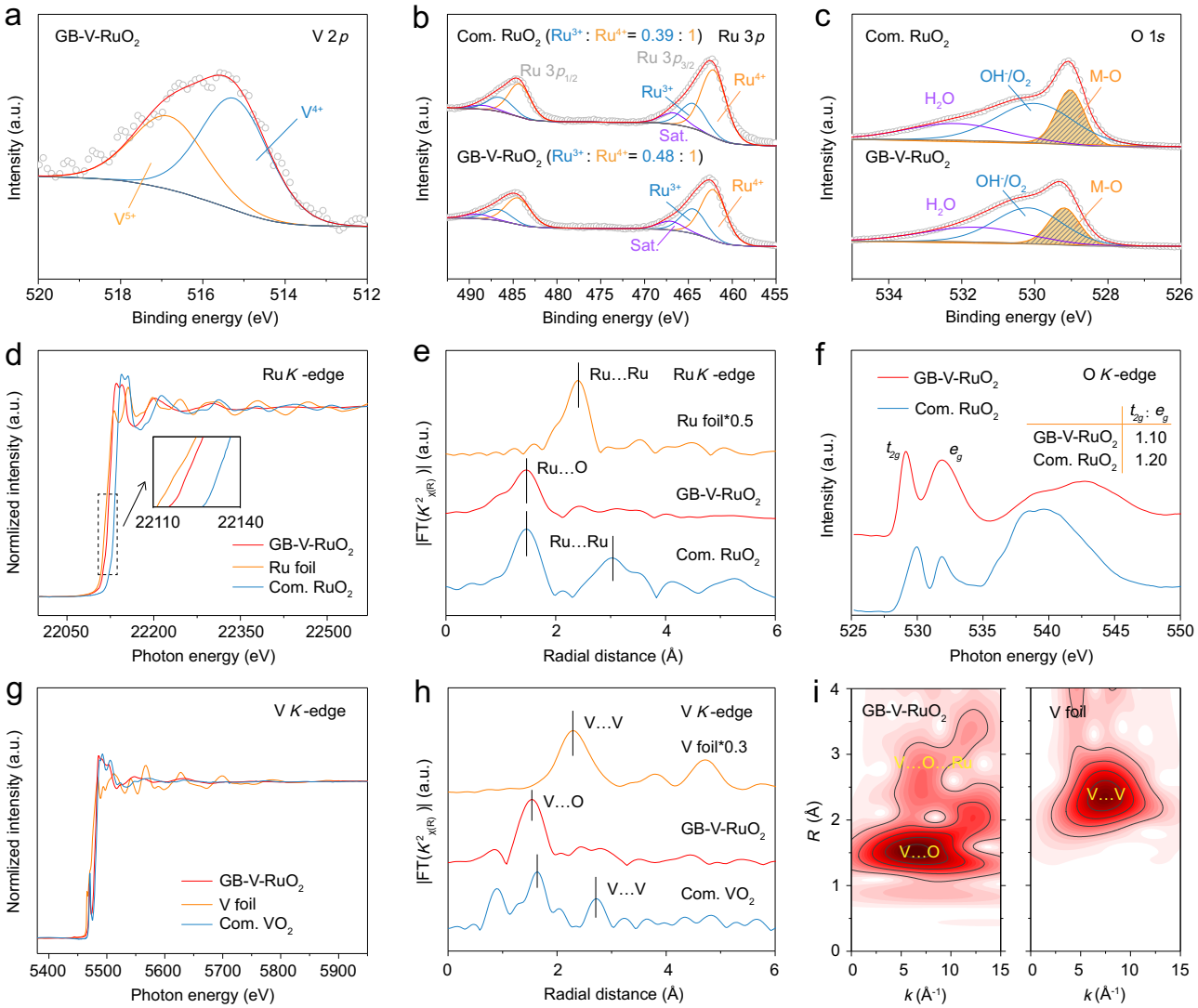

Fig. 2 | XPS and XAS characterization of GB-V-RuO$_2$. **a**-**c** V $2p_{3/2}$ (**a**), Ru $3p_{3/2}$ (**b**) and O 1*s* (**c**) XPS spectra of the GB-V-RuO$_2$ and Com. RuO$_2$ catalysts. **d**, (**e**) Normalized Ru K-edge XANES (**d**) and FT-K-edge EXAFS spectra (**e**) of GB-V-RuO$_2$. The data for Ru foil and Com. RuO$_2$ were also included for comparison. **f** O K-edge XAS spectra for GB-V-RuO$_2$ and Com. RuO$_2$. **g**, **h** Normalized V K-edge XANES (**g**) and FT-K-edge EXAFS spectra (**h**) for GB-V-RuO$_2$, with V foil and Com. VO$_2$ used as reference materials. **i**, k^3-weighted WT-EXAFS contour plot for (**i**) GB-V-RuO$_2$ and V foil. Source data for Fig. 2 are provided as a Source Data file.

EXAFS spectrum (Fig. 2h) for GB-V-RuO$_2$ displayed a peak at 1.52 Å in *R* space which could readily be ascribed to the V − O scattering path. Notably, the V − O peak position was close to that of the Ru–O peak (1.46 Å) in Com. RuO$_2$, confirming that V atoms replaced Ru atoms within RuO$_6$ motifs, which was expected to adjust the electronic structure of the remaining Ru–O bonds and thus enhance electrocatalyst activity. As exhibited in Fig. 2i, the k^3-weighted WT of the V K-edge EXAFS data was performed for GB-V-RuO$_2$ and V foil. The V K-edge WT-EXAFS spectra of GB-V-RuO$_2$ exhibited one intensity maxima, which could be attributed to a V − O scattering path (R = 1.51 Å and k = 6.63 Å^{-1}), with no V − V scattering path associated with V metal foil being observed.

Electrocatalytic performance of GB-V-RuO$_2$ for acidic OER

The OER performance of GB-V-RuO$_2$ was evaluated and compared with several benchmark electrocatalysts (Com. RuO$_2$ and Com. IrO$_2$) in 0.5 M H_2SO_4, where the linear sweep voltammetry (LSV) was adopted (see details in Electrochemical OER Measurement). As shown in Fig. 3a, Com. RuO$_2$ and Com. IrO$_2$ had overpotentials of 264 and 297 mV to reach 10 mA cm$^{-2}_{geo}$, respectively. In comparison, the GB-V-RuO$_2$ catalyst showed an improved OER activity, where an overpotential of only 159 mV was required to deliver 10 mA cm$^{-2}_{geo}$. Moreover, to reach the current density of 100 mA cm$^{-2}_{geo}$, the GB-V-RuO$_2$ catalyst achieved a minimum overpotential of 222 mV (~160 mV lower than that of Com. RuO$_2$). More importantly, the OER process on GB-V-RuO$_2$ could be maintained at industrial-level current densities (Fig. 3b), where low overpotentials of 270, 290 and 300 mV were required to deliver 500, 1000 and 1500 mA cm$^{-2}_{geo}$, respectively. As exhibited in Supplementary Fig. 12 and Table 2, GB-V-RuO$_2$ showed good OER activity at both low and high current densities compared with Com. RuO$_2$, Com. IrO$_2$ and most high-performance Ru/Ir-based catalysts recently reported for acidic OER. Moreover, the smallest Tafel slope of 58.5 mV dec^{-1} (Fig. 3c) further reflects the fast OER kinetics of GB-V-RuO$_2$ compared with Com. RuO$_2$ (85.1 mV dec^{-1}) and Com. IrO$_2$ (101.7 mV dec^{-1})[38,39]. The good OER performance of GB-V-RuO$_2$ catalyst was also confirmed using the glassy carbon as substrate (Supplementary Fig. 13), where the GB-V-RuO$_2$ catalyst still exhibits high OER activity compared with the commercial catalysts. To elucidate the relationship between the

https://doi.org/10.1038/s41467-025-59472-0

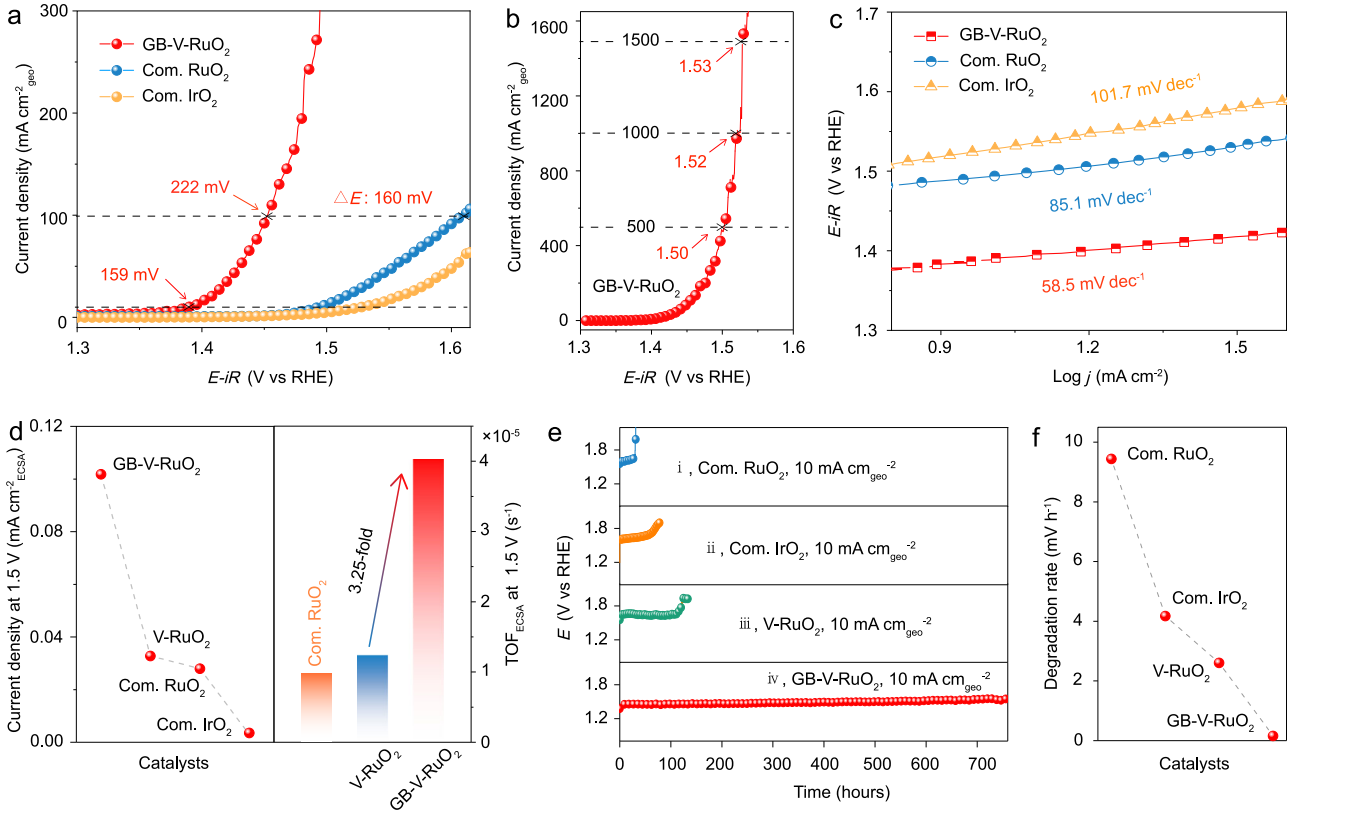

Fig. 3 | Investigations of OER activity and stability. a Representative LSV curves for GB-V-RuO_2, Com. IrO_2 and Com. RuO_2 in 0.5 M H_2SO_4. **b** LSV curve using GB-V-RuO_2 as the catalyst for acidic OER at high current density. **c** Corresponding Tafel slopes derived from **a**. **d** Comparison of the specific activity and TOF_{ECSA} values of GB-V-RuO_2, V-RuO_2, Com. IrO_2 and Com. RuO_2 at 1.5 V. **e** Chronopotentiometric curves for GB-V-RuO_2 during acidic OER, showing the improved stability of GB-V-RuO_2, in comparison with Com. RuO_2 and Com. IrO_2. The voltages were not *iR* compensated. **f** Comparison of the degradation rate of GB-V-RuO_2, V-RuO_2, Com. RuO_2 and Com. IrO_2 during long-term acidic OER tests. All the measurements were performed using carbon paper as substrate in 0.5 M H_2SO_4 (pH= 0.3 ± 0.01) at a scan rate of 5 mV s^{-1}. Source data for Fig. 3 are provided as a Source Data file.

catalytic activity and structure, we further evaluated the OER performance of V-RuO_2 and compared it with the GB-V-RuO_2 catalyst. As shown in Supplementary Table 3, GB-V-RuO_2 had a large electrochemical specific surface area (ECSA), ca. 28 times higher than that of V-RuO_2, which means a greatly increased number of active sites. Further, the LSV curves normalized by ECSA (Fig. 3d, Supplementary Fig. 14) verified the highest specific activity of GB-V-RuO_2 in the OER potential window compared to the V-RuO_2, Com. RuO_2 and Com. IrO_2. Meanwhile, the turnover frequency (TOF_{ECSA}, the TOF value normalized to ECSA) of GB-V-RuO_2 is ~3.25 times higher than that of V-RuO_2 catalyst (Supplementary Table 4), suggesting a higher intrinsic activity. Benefitting from the large ECSA (more active sites) and high intrinsic activity, GB-V-RuO_2 thus exhibited higher current density and TOF_{geo} (the TOF value normalized to geometric area, Supplementary Table 4) than that of V-RuO_2 within the tested OER potential region (Supplementary Figs. 15a). The large difference in acidic OER performance between GB-V-RuO_2 and V-RuO_2 (Supplementary Figs. 15b) suggested that GBs are important to regulating structure and boosting the catalytic activity of GB-V-RuO_2. Further, the catalytic activities of the electrocatalysts depended on the crystallization process and GB density (Supplementary Figs. 16–19). We found that as the density of GBs decreased, the ECSA and OER activity of the GB-V-RuO_2 series of catalysts progressively decreased (Supplementary Figs. 20–22). The relationship further demonstrated the important contribution of GBs to the improved OER activity of GB-V-RuO_2.

In addition to activity, the durability of catalysts is another important consideration for acidic oxygen evolution. Figure 3e shows the chronopotentiometric (CP) responses of GB-V-RuO_2, V-RuO_2, Com. RuO_2 and Com. IrO_2 catalysts in a homemade H-type cell at room temperature. The Com. RuO_2 and Com. IrO_2 showed poor durability under acidic conditions with a short operating time of less than 80 h at 10 mA cm^{-2}_{geo}. V-RuO_2 exhibited a slightly increased stability of 120 h. In contrast, the GB-V-RuO_2 catalyst showed significantly enhanced OER stability, where a long lifetime of ~760 h was achieved at 10 mA cm^{-2}_{geo}. To further verify the acidic stability of catalysts, the activity degradation rates were calculated (Fig. 3f). Notably, the GB-V-RuO_2 catalyst had a very low degradation rate of 0.16 mV h^{-1} during the 760-hour test. Contrastly, Com. RuO_2 (9.44 mV h^{-1}), Com. IrO_2 (4.18 mV h^{-1}), and V-RuO_2 (2.61 mV h^{-1}) exhibited much higher degradation rates. In addition, the GB-V-RuO_2 catalyst can also operate stably for more than 60 h at 100 mA cm^{-2}_{geo} (Supplementary Fig. 23). However, rapid voltage climbs were observed in a short time for GB-RuO_2 and Com. RuO_2, indicating their comparatively poor acid durability at high current density. The good stability of GB-V-RuO_2 was further confirmed by the time-dependent current density curve (Supplementary Fig. 24). Due to its good acid OER activity and durability, the GB-V-RuO_2 catalyst is comparable with those high-performance Ru/Ir-based catalysts for acidic OER, as shown in Supplementary Table 2. In addition, a simple PEMWE device was assembled using the GB-V-RuO_2 catalyst as the anode (Supplementary Fig. 25), where the GB-V-RuO_2 catalyst also exhibited a high PEM performance. Specifically, only 1.400, 1.472 and 1.577 V are required for the current densities of 0.2, 0.5, and 1.0 A cm^{-2}_{geo}, respectively. The PEMWE device can also operate steadily for 500 h at 0.2 A cm^{-2}_{geo}, significantly exceeding the PEMWE devices using GB-RuO_2 and Com. RuO_2. Therefore, the high performance of the PEMWE device based on GB-V-RuO_2 further demonstrates its great

potential for future practical applications. Furthermore, cyclic voltammetry (CV) tests were conducted to analyze the oxidation behavior of Ru sites during OER (Supplementary Fig. 26). As can be seen, Com. RuO_2 displayed two sets of redox peaks near 0.60 and 1.25 V, which can be readily attributed to Ru^{3+}/Ru^{4+} and $Ru^{4+}/Ru^{\delta+,\delta>4}$, respectively[40,41]. For the GB-V-RuO_2 catalyst, a significantly increased Ru^{3+}/Ru^{4+} signal area was observed, suggesting that the oxidation state of Ru in GB-V-RuO_2 varied between +3 and +4 during the OER process[42]. Furthermore, peaks assigned to $Ru^{4+}/Ru^{\delta+,\delta>4}$ disappeared for GB-V-RuO_2, indicating that the over-oxidation of Ru sites was effectively suppressed during the acidic OER, thus stabilizing the structure of GB-V-RuO_2 and enhancing its OER durability. The university of this synthetic modulation strategy in optimizing the electronic environment of local Ru −O bonding at the GBs and thus improving the OER performance has been also well demonstrated, as shown in Supplementary Note 2 and Supplementary Figs. 27–29.

We carefully studied the composition and structure of the GB-V-RuO_2 catalyst after the stability test to gain deeper insight into its robust durability. As shown in Supplementary Fig. 30, XRD revealed that the peaks attributed to rutile-structured RuO_2 were still retained after the long-term acidic OER testing. The slight broadening of diffraction peaks after OER suggested some mild surface corrosion of the catalyst had occurred. AC-HAADF STEM images (Supplementary Figs. 31 and 32) showed that the original morphology of GB-V-RuO_2 was retained during OER, as well as the uniform distribution of Ru, V and O elements. The magnified AC-HAADF STEM image further showed that abundant GBs still existed along with the crystalline RuO_2 lattice arrays in GB-V-RuO_2 after OER. The surface chemical information from XPS analysis revealed almost no V in the near surface region of the used catalysts (Supplementary Fig. 33), indicating that V was leached from the surface (depth of ~10 nm) of the GB-V-RuO_2 catalyst. Moreover, up to 41.3 % of the V in the parent GB-V-RuO_2 was dissolved into the electrolyte (Supplementary Table 5), which was also verified by the EDX line scanning profiles (Supplementary Fig. 32). The loss of V atoms leads to the overoxidation of active Ru site and its corresponding dissociation, and this is likely responsible for the modest activity degeneration during the long-term testing. The core-level Ru 3 d XPS spectra for used GB-V-RuO_2 (Supplementary Fig. 34) showed a decreased ratio of Ru^{3+} to Ru^{4+} (0.36:1) on the catalyst surface, implying that more high-valent Ru^{4+} were formed in the oxidation voltage window.

Operando spectroelectrochemical measurements exploring the OER pathway

We next conducted operando EIS, ATR-SEIRAS IR and DEMS analyses to investigate the oxygen evolution reaction mechanism used by the different catalysts. Firstly, to reveal the interfacial charge transfer behavior under different applied biases, operando EIS tests were carried out. The Bode plot (Fig. 4a, b and Supplementary Fig. 35) reflects the OER reaction kinetics, manifested by a decrease in low-frequency peaks and a shift of phase angle to higher frequencies with increasing bias[43]. The low-frequency phase angular peaks are related to the surface charge conduction of the catalyst[44]. Generally, the smaller the phase angle of the low-frequency region is, the faster the electron transfer of OER is. Compared with V-RuO_2 and Com. RuO_2, the GB-V-RuO_2 catalyst exhibited the smallest phase angle in the low-frequency region with a narrow phase transition peak interval of 1.35-1.5 V, indicating the fastest charge transfer rate on the catalyst surface. The corresponding Nyquist plots further confirmed the fast charge transfer process on the surface of GB-V-RuO_2 catalyst (Supplementary Fig. 36), which is consistent with its good OER performance. Isotope-labeled operando DEMS measurements were further performed to identify the OER pathway on GB-V-RuO_2. For comparison, the V-RuO_2 was used as a reference catalyst to reveal the influence of GBs on the OER process. Figure 4d shows the operando DEMS apparatus, with the evolved O_2 products being analyzed using gas chromatography. As shown in Supplementary Figs. 37 and 38, catalysts were firstly ^{18}O-labeled using multiple LSV and CV cycles (1.1-1.5 V versus RHE) in a $H_2{}^{18}O$-containing electrolyte (0.5 M H_2SO_4). After that, the ^{18}O-labeled catalysts were thoroughly washed with $H_2{}^{16}O$ deionized water, followed by four LSV cycles in the $H_2{}^{16}O$ electrolyte. As depicted in Fig. 4c, when the voltage reached the OER region, the signals of $^{32}O_2{}^{34}$,O_2 and $^{36}O_2$ products were detected using GB-V-RuO_2 and V-RuO_2 as the anode catalysts. As previously reported[22,25], the O_2 speciation of products can be used to distinguish the AEM and LOM (Fig. 5e). The composition of the gaseous O_2 products was further quantified and compared using MS. As shown in Fig. 4f^{32},O_2 was the main product along with small amounts of $^{34}O_2$ and $^{36}O_2$, indicating an AEM-dominant oxygen evolution on the catalyst surface (Supplementary Fig. 39)[45,46]. GB-V-RuO_2 evolved negligible amounts of $^{34}O_2$ and $^{36}O_2$, suggesting that GBs can effectively inhibit the LOM path (Supplementary Fig. 40) and stabilize the catalyst structure[47]. Also, operando DEMS spectra (Supplementary Fig. 41) collected from GB-RuO_2 showed that an AEM-dominant oxygen evolution occurred on GB-RuO_2, indicating the introduction of GBs can effectively improve the catalytic activity of RuO_2 without activating LOM. To further verify the OER pathways, the oxygen intermediate species generated on the electrocatalysts during OER were identified using operando ATR-SEIRAS IR analysis. Figure 4g shows the operando ATR-SEIRAS IR spectra collected from GB-V-RuO_2 as a function of the applied step voltage. Several absorption peaks centered at 1019, 1200 and 3300 cm^{-1} were observed as the voltage increased. The absorption peaks centered at 1200 and 3300 cm^{-1} are attached to *OOH and *OH intermediates (Supplementary Table 6) formed during the AEM pathway, respectively[48,49]. Similar spectral changes were also observed on V-RuO_2 (Fig. 4h), except for the significantly enhanced peak at 1019 cm^{-1}, which is assigned to *OO, suggesting the co-existence of a LOM pathway on that catalyst[50,51]. As is well known, LOM processes can contribute partly to high intrinsic OER activity. However, if the loss rate of lattice O is higher than its replenishing rate, the dynamic accumulation of O vacancies can weaken the binding of neighbouring Ru atoms, thus leading to the dissolution of Ru active sites and bulk structure destabilization. In view of this, the ratio of peak intensities of *OO and *OOH was carefully analyzed and compared for GB-V-RuO_2 and V-RuO_2. As shown in Fig. 4i, in the OER potential range, GB-V-RuO_2 had a much smaller ratio of I_{*OO}/I_{*OOH}, indicating the participation of lattice O was inhibited compared with V-RuO_2 and the reaction path over GB-V-RuO_2 mainly involved AEM, consistent with the operando DEMS results. In summary, the operando spectroelectrochemical measurements revealed an AEM-dominant O_2 evolution process on the GB-V-RuO_2 catalyst, with GBs effectively inhibiting the LOM path and stabilizing the catalyst structure, thus resulting in fast OER reaction kinetics and good durability, in good agreement with the OER performance determined experimentally.

DFT calculations

To elucidate the synergistic role of GBs and V-doping in the OER performance of GB-V-RuO_2, DFT calculations were performed to reveal the intrinsic mechanism. Our calculations indicated that the (110) crystal plane of RuO_2 is the most active for acidic OER (Supplementary Fig. 42), which is consistent with the reported literatures[1,12,20]. Thus, (110) facet plane was selected as the computational model to perform the following calculations (Supplementary data 1, 2 and 3). According to the experimental results, three models were constructed for the calculations, including RuO_2 (110), V-RuO_2 (110) and GB-V-RuO_2, as displayed in Fig. 5a and Supplementary Fig. 43. Firstly, it was confirmed that V-doping to replace Ru_{BRI} site was more thermodynamically favored (Supplementary Fig. 44), with a lower doping energy of 0.30 eV. As such, V-doping into Ru_{BRI} site was selected for the subsequent calculations, where neighboring Ru_{CUS} site acted as the active site for OER (See Fig. 5b and Supplementary Fig. 45). To clarify the

https://doi.org/10.1038/s41467-025-59472-0

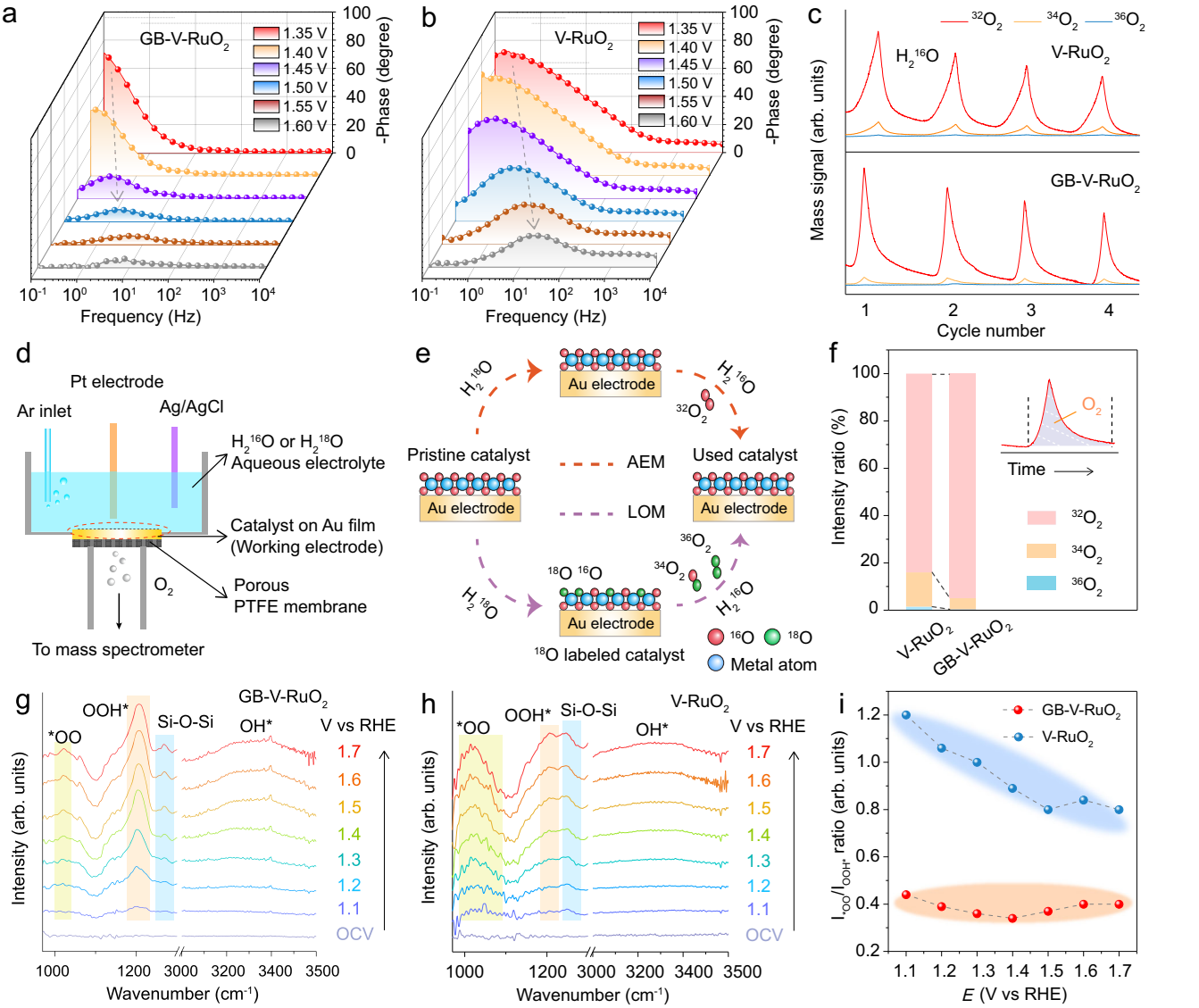

Fig. 4 | Combined operando spectroscopic analyses to identify the OER pathway. a, b Operando EIS spectra for GB-V-RuO_2 (**a**) and V-RuO_2 (**b**) during OER from 1.35 to 1.6 V versus RHE. **c** Operando DEMS signals of the generated $^{32}O_2{}^{34},O_2$ and $^{36}O_2$ versus time when performing LSV tests in a $H_2{}^{16}O$-based acidic electrolyte for ^{18}O-labeled GB-V-RuO_2 and V-RuO_2. **d** Schematic illustration of the operando DEMS apparatus. **e** Diagram of the DEMS measurements involving the AEM and LOM pathways, respectively. **f** Detailed comparison between $^{32}O_2{}^{34},O_2$ and $^{36}O_2$ signals for the experiment in (**c**). Inset shows the way to quantify oxygen through integrating the mass spectrometer signals. **g, h** Operando ATR-SEIRAS IR analysis spectroscopic investigation for GB-V-RuO_2 (**g**) and V-RuO_2 (**h**) with potentials (versus RHE) applied from 1.1 to 1.7 V. **i** Detailed comparison of the ratio of I_{*OO} /I_{*OOH} signal intensity. Source data for Fig. 4 are provided as a Source Data file.

influence of GBs and V doping on the electronic structure of RuO_2, the density of states (DOS) of the active sites was then calculated (Supplementary Fig. 46). Compared with RuO_2 (-1.02 eV), the *d*-band center of V-RuO_2 (-1.11 eV) decreased after V-doping, evidencing a modified electronic structure. The *d*-band center of GB-V-RuO_2 shifted further away from the Fermi level (-1.73 eV), which will weaken the binding energy of oxygen intermediates according to *d*-band center theory[52]. A weaker *O binding energy for GB-V-RuO_2 agreed with the negative *d*-band center shift, which was expected to enhance the OER activity. Next, charge density difference calculations and Bader charge analyses were performed, as displayed in Supplementary Fig. 47. Compared to pristine RuO_2, a significant charge rearrangement around the active site for V-RuO_2 and V-GB-RuO_2 was observed, which was responsible for the improved OER activity of these catalysts. Further, the number of electrons transferred after *O adsorption was calculated for V-RuO_2 and GB-V-RuO_2 to uncover the role of GBs (Supplementary Fig. 48). Compared with V-RuO_2 (0.43 e^-), less electron transfer occurred for GB-V-RuO_2 (0.36 e^-), which is beneficial to have acted to reduce the binding energy of *O and further enhance its OER activity. The electronic structure analyses thus explain the activity difference of these three catalysts.

Next, the OER performance of the three model catalysts was evaluated, considering both the AEM and LOM pathways. The potential determining step (PDS) was explored. As shown in Fig. 5b, for the AEM mechanism, the PDS of RuO_2 and V-RuO_2 was the third reaction step (*O → *OOH) with high theoretical overpotentials of 0.65 and 0.66 V, respectively. But for V-GB-RuO_2, the PDS transforms to the last step (*OOH → O_2) with a low overpotential of only 0.41 V, confirming that GBs can significantly boost the activity of V-RuO_2. As for the LOM path (Fig. 5b and Supplementary Figs. 49 and 50), the overpotentials of RuO_2, V-RuO_2 and GB-V-RuO_2 were 1.56, 1.75 and 1.63 V, respectively. All overpotentials for the LOM pathway were higher than those of the AEM pathway, suggesting a dominant AEM path on the three catalysts. In order to further explore the selectivity between AEM and LOM

https://doi.org/10.1038/s41467-025-59472-0

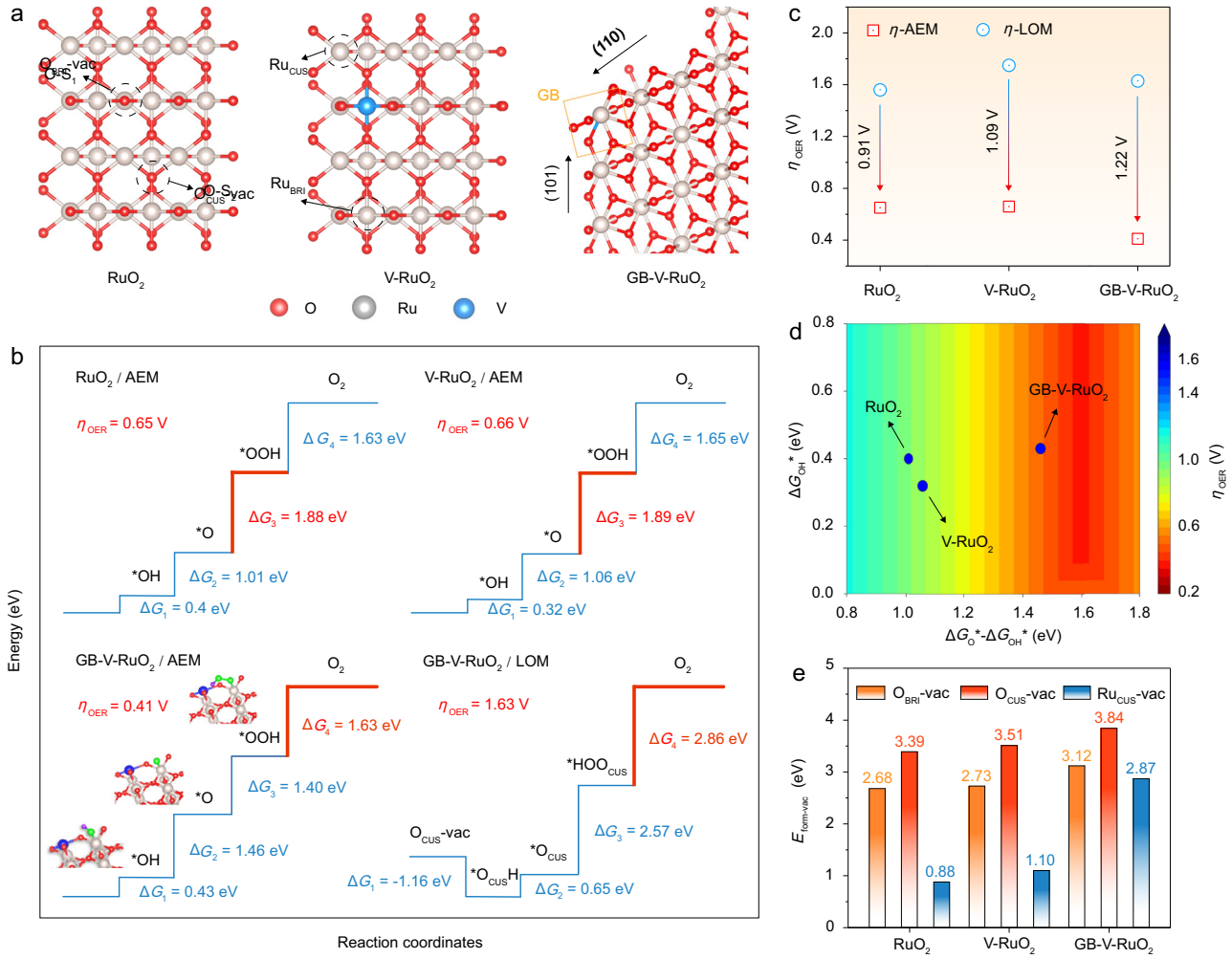

Fig. 5 | DFT calculations investigating the OER mechanism. a RuO_2 (110), V-RuO_2 and GB-V-RuO_2 (110) models. **b** Gibbs free energy diagrams for OER based on AEM and LOM pathways over RuO_2, V-RuO_2 and GB-V-RuO_2. **c** Overpotential difference for AEM and LOM pathways on RuO_2, V-RuO_2 and GB-V-RuO_2. **d** OER volcano plot of overpotential with $\Delta G_{*O} - \Delta G_{*OH}$ and ΔG_{OH} as descriptors. **e** Comparison of formation energies of Ru_{CUS} and O vacancies on RuO_2, V-RuO_2 and GB-V-RuO_2 surfaces. Source data for Fig. 5 are provided as a Source Data file.

mechanisms, the overpotential difference between the two pathways was calculated for each catalyst. As illustrated in Fig. 5c, compared with RuO_2 (0.91 V), V-RuO_2 had a higher overpotential difference (1.09 V). The largest difference of 1.22 V was seen for GB-V-RuO_2, indicating a high AEM selectivity after introducing GBs. The activity origin of these three catalysts was further explored. According to previous report[53], a linear scaling relationship between $\Delta G_{*O} - \Delta G_{*OH}$ and ΔG_{*OH} exists for AEM. As such, we plotted ΔG_{*OH} against $\Delta G_{*O} - \Delta G_{*OH}$ in Fig. 5d, finding that GB-V-RuO_2 was closer to the peak in the η volcano diagram, which indicates that GB-V-RuO_2 has a near-ideal binding energy of OER reaction intermediates, further confirming the synergistic role of V-doping and GBs in enhancing the OER. In addition, we also found that the strain effect at the GBs has a limited effect on the OER activity (Supplementary Fig. 51), where the significantly promoted OER activity of GB-V-RuO_2 is intrinsically attributed to the regulated electronic structure of active Ru-O-V motifs at the GBs. Lastly, the stability of these three catalysts was evaluated by calculating the formation energy of O and Ru_{CUS} vacancies, with the results summarized in Fig. 5e. It can be observed that the formation energy of O_{vac} and Ru_{vac} followed the order of GB-V-RuO_2 > V-RuO_2 > RuO_2, which illustrates that the coexistence of V and GBs contributes to the long lifetime of GB-V-RuO_2. Also, based on the experimental results, the leaching of abundant V atoms in the parent GB-V-RuO_2 (Supplementary Table 5) results in the activity degeneration during the long-term test. In order to evaluate the effect of V leaching on the OER activity of GB-V-RuO_2, the theoretical calculation about the OER activity of GB-V-RuO_2 with V vacancy (GB-V-RuO_2/V_{vac}) was calculated, as shown in Supplementary Fig. 52. Compared with GB-V-RuO_2, GB-V-RuO_2/V_{vac} exhibits the similar potential determining step, but the free energy barrier of GB-RuO_2/V_{vac} is as high as 2.02 eV. This correspondingly leads to a higher theoretical overpotential of GB-V-RuO_2/V_{vac} (0.79 V) than that of GB-V-RuO_2 (0.41 V), in agreement with the experimental results. In addition, the V site located at GBs also exhibits a larger demetallation energy than that at the Ru (110) basal plane (Supplementary Fig. 53), which means that the V site at GBs is more stable, further confirming that the formation of GBs can alleviate V leaching and thus ensure the good stability of GB-V-RuO_2. Our theoretical calculations agree well with the experimental results and reveal that GBs and V dopants can remarkably improve the acidic OER performance of RuO_2-based catalysts.

Discussion

In summary, abundant grain boundaries were successfully constructed into V-doped RuO_2 catalyst, achieving highly active and acid-stable OER electrocatalysis. Low overpotentials of 159 and 300 mV were required to reach 10 and 1500 mA cm^{-2}_{geo}, respectively. The GB-V-RuO_2 catalyst can operate stably for ~760 h at 10 mA cm^{-2}_{geo} under acidic

conditions, and then the leaching of most V dopants mainly led to the deactivation. Operando EIS, ATR-SEIRAS FTIR and DEMS measurements revealed that the introduction of GBs can effectively prevent lattice O from participating in OER, resulting in an AEM-dominant OER pathway over the entire OER potential window even at high current densities. DFT analyses verified that introducing V atom dopants and GBs modulated the electronic structure of RuO_2 for more efficient OER activity. Importantly, a large theoretical voltage difference between the LOM and AEM pathways allowed the GB-V-RuO_2 catalyst to strictly follow an AEM path in acidic OER. Moreover, GBs significantly enhanced the stability of GB-V-RuO_2 catalyst during OER by alleviating V leaching. Consequently, very high acidic OER activity and good durability were realized.

Methods

Materials

All chemicals were purchased directly from commercial suppliers and used without further purification. The $RuCl_3{\cdot}3H_2O$, Water−^{18}O ($H_2{}^{18}O$), Com. RuO_2 (99.95%) and IrO_2 (99.95%) were purchased from Adamas Reagent (Shanghai) Co., Ltd. The VCl_3 and 5 wt% Nafion® ionomer were purchased from Shanghai Aladdin Biochemical Technology Co.,Ltd. The Com. Pt/C (40 wt% Pt), titanium felt and carbon paper were purchased from Suzhou Sinero Technology Co.,Ltd. The Nafion 115 membrane was purchased from DuPont Co.

Synthesis of catalysts

The catalysts were synthesized using a thermal-driven cation exchange strategy. Firstly, an aqueous solution containing 0.015 g of VCl_3 and 0.30 g of $RuCl_3{\cdot}3H_2O$ in 150 mL of water was prepared. The aqueous solution was heated in the Teflon-lined autoclave at 200 °C for several hours. The obtained precipitate was washed and then dried. The collected powders were then calcined at 350, 400, 500, 600 or 700 °C for 4 h, respectively. The product obtained at 350 °C is denoted herein as GB-V-RuO_2, whilst the product obtained at 700 °C is denoted herein as V-RuO_2. The GB-RuO_2 catalyst was obtained using a similar process to GB-V-RuO_2, but without the addition of VCl_3.

Characterization

A Rigaku MiniFlex600 equipment (a Cu K_α X-ray source) was used to obtain the wide-angle powder XRD data. Aberration-corrected scanning transmission electron microscope (USA) was used to collect the HAADF-STEM and bright field images. A Gatan Enfina electron energy-loss spectrometer and a Gatan EDAX energy-dispersive X-ray system were used. XPS analyses used a Kratos AXIS Ultra DLD spectrometer. The Ru and V loadings in the samples were determined by ICP-OES (Agilent 5110). The Shanghai Synchrotron Radiation Facility offered the service for testing XAS measurements in transmission mode. We employed a Si (111) double-crystal monochromator to control the X-ray photon energy. The metallic Ru and V foils were used for the energy calibration. Background normalization/subtraction routines were carried out using Athena software.

Electrochemical OER measurement

The electrolyte is 0.5 M H_2SO_4. The concentrated sulfuric acid (98%) and deionized water were used to prepare the electrolyte (0.5 M H_2SO_4). The pH of the electrolyte is 0.3 ± 0.01[18]. Acidic OER tests on GB-V-RuO_2 and the other reference electrocatalysts were carried out at room temperature. A homemade three-electrode cell was adopted, which consists of a working electrode (catalyst-modified carbon paper (area 0.25 cm^2_{geo}) / glassy carbon electrode (area 0.1963 cm^2_{geo})), a counter electrode (graphite rod) and a reference electrode (saturated calomel electrode (SCE)). An electrochemical workstation (model number CHI660E) from Shanghai, China was adopted to conduct all electrochemical tests. To prepare the working electrodes, dispersions consisting of 5 mg of electrocatalyst, 20 µL of Nafion solution (5 wt.%) and 480 µL deionized water were prepared. After the ultrasonic treatment, the homogeneous electrocatalyst ink was applied on the working electrode, after which the resulting modified working electrode was allowed to dry naturally in air. The mass loadings of the electrocatalysts on glassy carbon and carbon paper were controlled at approximately 0.5 and 1.0 mg cm^{-2}_{geo}, respectively. Using the equation ($E_{RHE} = E_{SCE} + E^{\theta}_{SCE} + 0.059\times pH - 1.23$ V, where E_{RHE} and E^{θ}_{SCE} are potentials versus RHE, with $E^{\theta}_{SCE} = 0.241$ V.) to obtain the overpotential against the reversible hydrogen electrode (RHE)[22]. The SCE electrode was calibrated under an H_2 atmosphere using a Pt wire as the working electrode[18,45]. For comparison, Com. RuO_2 (Adamas, 99.95%) and IrO_2 (Adamas, 99.95%) were obtained. The OER performance of V-RuO_2 and other reference electrocatalysts were all tested under the same conditions to allow meaningful comparison of their intrinsic catalyst activity and stability. Linear sweep voltammetry (LSV) tests of (sweep rate: 5 mV s^{-1}) were used. To evaluate the OER activity at a large current density (> 1 A cm_{geo}^{-2}), the Autolab electrochemical analyzer configured with BOOSTER10A was used. The voltage range was 1.1–1.7 V versus RHE. The solution resistance (~4.5 Ω) was tested at an open circuit voltage. A 95% *iR* compensation was employed. We employed electrochemical impedance spectroscopy (EIS, 0.1 ~100 KHz). The CV method at different scan rates (1.041–1.141 V versus RHE with no Faradaic processes) was used to obtain electrochemically active surface areas (ECSA). A linear fit was applied to plots of current density difference versus sweep rate was carried out to calculate double-layer capacitance (C_{dl}), in which the slope is the C_{dl} value. A homemade H-type electrolytic cell was used to conduct the long-term stability of GB-V-RuO_2 during OER at different current densities[18].

In situ EIS measurements

The in-situ EIS tests (1.35 to 1.6 V versus RHE) were carried out in 0.5 M H_2SO_4, as previously reported[40]. The frequency range was 0.1 to 10,000 Hz.

Operando ATR-SEIRAS IR measurements

Operando attenuated total reflection surface-enhanced infrared spectroscopy (ATR-SEIRAS IR) data were recorded using the previous method[13,18]. The electrocatalysts were deposited on the Au-coated Si prism and used as working electrodes. Before ATR-SEIRAS IR measurements, a potential was applied to the as-constructed working electrode for a period of time until reliable signals were obtained. Background curves were collected under open circuit conditions. The resolution was 4 cm^{-1}.

Operando DEMS measurements with isotope labelling

Operando DEMS experiments were conducted on a homemade three-electrode cell[18]. For the isotope labelling investigations, an electrolyte (0.5 M H_2SO_4) containing $H_2{}^{18}O$ was used to label the electrocatalyst at voltages from 1.1 to 1.5 V versus RHE. Then, the ^{18}O-labelled electrocatalyst was subjected to multiple LSV cycles in an electrolyte (0.5 M H_2SO_4) with $H_2{}^{16}O$ as a solvent, and the gaseous products were detected by mass spectrometry.

Computational details

The Vienna ab initio simulation package (VASP 5.4.4) was adopted here[54]. The exchange-correlation energy was explored via the Perdew-Burke-Ernzerhof function based on the theory of Generalized Gradient Approximation[55]. Moreover, we studied the expansion of the electronic eigenfunctions, where a kinetic energy cutoff of 450 eV was considered using the projector-augmented wave method[56]. Values of 0.03 eV $Å^{-1}$ and 10^{-5} eV were set for the force convergence threshold and total energy, respectively. Using the empirical correction of the DFT + D3 scheme investigated Van der Waals interactions[57]. The

vacuum layer was at least 15 A in the z direction to minimize possible interactions between slabs. The electron transfer was calculated via Bader charge analysis[58]. The Brillouin zone was sampled with a 3 × 3 × 1 k-points grid for the RuO_2 and V-RuO_2 via the Monkhorst-Pack scheme, while 2 × 2 × 1 k-points grid was utilized for the V-GB-RuO_2 to avoid too many atoms in the model. Denser 5 × 5 × 1 and 7 × 7×1 k points were taken for static self-consistent calculations and electronic structure calculations.

The Gibbs free energy change (ΔG) was estimated according to the following Eq. (1), where the computational hydrogen electrode (CHE) model was employed for imitating the OER reactions[59]:

$$\Delta G = \Delta E_{ZPE} + \Delta E + \Delta G_{pH} + \Delta G_U - T\Delta S \quad (1)$$

in which ΔE_{ZPE} signifies the difference in zero-point energy at 298.15 K, which can be calculated from vibrational frequencies, between the products and the reactants. The values of ΔE were obtained from the total energies. The effects of the electrode pH and applied voltage were corrected using the ΔG_{pH} and ΔG_U terms, respectively. ΔS is the entropy change and was obtained in a similar manner to ΔE_{ZPE}; The vibrational frequencies of free molecules and entropy values were obtained from the NIST database[60].

The formation energy of an O vacancy and Ru vacancy were calculated by the following Eq. (2):

$$E_{vac-form} = E_{vac} + \mu O/\mathrm{Ru} - E_{pri} \quad (2)$$

where E_{vac}, $\mu_{O/Ru}$ and E_{pri} are the energy of catalysts with O or Ru vacancy, the chemical potential O/Ru referenced to O_2 gas and a Ru crystal, and the energy of the pristine catalyst, respectively.

The doping energy of V was calculated by the following Eq. (3):

$$E_{dop} = E_{V-RuO2} + \mu_{Ru} - E_{RuO2} - \mu_V \quad (3)$$

where $E_{V\text{-}RuO2}$, E_{RuO2}, μ_{Ru} and μ_V are the energy of V-RuO_2, RuO_2 and the chemical potential of Ru and V atoms, respectively.

For the construction of grain boundaries, we developed an effective strategy to build them. Firstly, a 4*4 supercell with six layers of RuO_2 (101) facets was constructed. Next, based on the built (101) facet, the (110) facet was cut, and the junction between (101) facet and (110) facet was defined as the grain boundary of these two facets. This construction method can maintain the stability of grain boundary during the calculation process.

Data availability

All data supporting this study is available in the article and the Supplementary Information. Source data are provided within this paper. Source data are provided with this paper.

References

1. Wu, Z.-Y. et al. Non-iridium-based electrocatalyst for durable acidic oxygen evolution reaction in proton exchange membrane water electrolysis. *Nat. Mater.* **22**, 100–108 (2023).
2. Chang, J. et al. Synthesis of ultrahigh-metal-density single-atom catalysts via metal sulfide-mediated atomic trapping. *Nat. Synth.* **3**, 1427–1438 (2024).
3. Kong, S. et al. Acid-stable manganese oxides for proton exchange membrane water electrolysis. *Nat. Catal.* **7**, 252–261 (2024).
4. Oener, S. Z., Bergmann, A. & Cuenya, B. R. Designing active oxides for a durable oxygen evolution reaction. *Nat. Synth.* **2**, 817–827 (2023).
5. Wang, Q. et al. Long-term stability challenges and opportunities in acidic oxygen evolution electrocatalysis. *Angew. Chem., Int. Ed.* **135**, e202216645 (2023).
6. Hu, C. et al. Misoriented high-entropy iridium ruthenium oxide for acidic water splitting. *Sci. Adv.* **9**, eadf9144 (2023).
7. Wen, Y. et al. Stabilizing Highly Active Ru Sites by Suppressing Lattice Oxygen Participation in Acidic Water Oxidation. *J. Am. Chem. Soc.* **143**, 6482–6490 (2021).
8. Shi, Z. et al. Enhanced Acidic Water Oxidation by Dynamic Migration of Oxygen Species at the Ir/Nb_2O_{5-x} Catalyst/Support Interfaces. *Angew. Chem., Int. Ed.* **61**, e202212341 (2022).
9. Zhou, L. et al. Stabilizing non-iridium active sites by non-stoichiometric oxide for acidic water oxidation at high current density. *Nat. Commun.* **14**, 7644 (2023).
10. Raman, A. S. & Vojvodic, A. Providing Atomistic Insights into the Dissolution of Rutile Oxides in Electrocatalytic Water Splitting. *J. Phys. Chem. C.* **126**, 922–932 (2022).
11. Klyukin, K., Zagalskaya, A. & Alexandrov, V. Role of Dissolution Intermediates in Promoting Oxygen Evolution Reaction at RuO_2 (110) Surface. *J. Phys. Chem. C.* **123**, 22151–22157 (2019).
12. Jin, H. et al. Dynamic rhenium dopant boosts ruthenium oxide for durable oxygen evolution. *Nat. Commun.* **14**, 354 (2023).
13. Chang, J. et al. Oxygen Radical Coupling on Short-Range Ordered Ru Atom Arrays Enables Exceptional Activity and Stability for Acidic Water Oxidation. *J. Am. Chem. Soc.* **146**, 12958–12968 (2024).
14. Lin, Y., Dong, Y., Wang, X. & Chen, L. Electrocatalysts for the Oxygen Evolution Reaction in Acidic Media. *Adv. Mater.* **35**, 2210565 (2023).
15. Dickens, C. F. & Nørskov, J. K. A Theoretical Investigation into the Role of Surface Defects for Oxygen Evolution on RuO_2. *J. Phys. Chem. C.* **121**, 18516–18524 (2017).
16. Wang, X. et al. Electronic Structure Modulation of RuO_2 by TiO_2 Enriched with Oxygen Vacancies to Boost Acidic O_2 Evolution. *ACS Catal.* **12**, 9437–9445 (2022).
17. Liu, S. et al. Structurally-Distorted RuIr-Based Nanoframes for Long-Duration Oxygen Evolution Catalysis. *Adv. Mater.* **35**, 2305659 (2023).
18. Wu, H. et al. Atomically engineered interfaces inducing bridging oxygen-mediated deprotonation for enhanced oxygen evolution in acidic conditions. *Nat. Commun.* **15**, 10315 (2024).
19. Wang, Y. et al. Breaking the Ru–O–Ru Symmetry of a RuO_2 Catalyst for Sustainable Acidic Water Oxidation. *Angew. Chem., Int. Ed.* **63**, e202316903 (2024).
20. Wang, J. et al. Single-site Pt-doped RuO_2 hollow nanospheres with interstitial C for high-performance acidic overall water splitting. *Sci. adv.* **8**, eabl9271 (2022).
21. Du, K. et al. Interface engineering breaks both stability and activity limits of RuO_2 for sustainable water oxidation. *Nat. Commun.* **13**, 5448 (2022).
22. Song, H. et al. RuO_2–CeO_2 Lattice Matching Strategy Enables Robust Water Oxidation Electrocatalysis in Acidic Media via Two Distinct Oxygen Evolution Mechanisms. *ACS Catal.* **14**, 3298–3307 (2024).
23. Xu, Y. et al. Strain-modulated Ru-O Covalency in Ru-Sn Oxide Enabling Efficient and Stable Water Oxidation in Acidic Solution. *Angew. Chem., Int. Ed.* **63**, e202316029 (2024).
24. He, W. et al. Grain-Boundary-Rich RuO_2 Porous Nanosheet for Efficient and Stable Acidic Water Oxidation. *Angew. Chem. Int. Ed.* e202405798 (2024).
25. Shi, Z. et al. Confined Ir single sites with triggered lattice oxygen redox: Toward boosted and sustained water oxidation catalysis. *Joule* **5**, 2164–2176 (2021).
26. Zhang, N. & Chai, Y. Lattice oxygen redox chemistry in solid-state electrocatalysts for water oxidation. *Energy Environ. Sci.* **14**, 4647–4671 (2021).
27. Fabbri, E. & Schmidt, T. J. Oxygen Evolution Reaction—The Enigma in Water Electrolysis. *ACS Catal.* **8**, 9765–9774 (2018).

28. Hwang, J. et al. Perovskites in catalysis and electrocatalysis. *Science* **358**, 751–756 (2017).
29. Lu, S.-Y. et al. Synthetic tuning stabilizes a high-valence Ru single site for efficient electrolysis. *Nat. Synth.* **3**, 576–585 (2024).
30. Jin, H. et al. Safeguarding the RuO_2 phase against lattice oxygen oxidation during acidic water electrooxidation. *Energy Environ. Sci.* **15**, 1119–1130 (2022).
31. Shi, Z. et al. Customized reaction route for ruthenium oxide towards stabilized water oxidation in high-performance PEM electrolyzers. *Nat. Commun.* **14**, 843 (2023).
32. Zhang, D. et al. Construction of Zn-doped RuO_2 nanowires for efficient and stable water oxidation in acidic media. *Nat. Commun.* **14**, 2517 (2023).
33. Li, F. & Baek, J.-B. Active site engineering accelerates water electrolysis. *Nat. Synth.* **3**, 558–559 (2024).
34. Wang, J. et al. Exceptionally active and stable RuO_2 with interstitial carbon for water oxidation in acid. *Chem* **8**, 1673–1687 (2022).
35. Cui, T. et al. Facilitating an Ultrastable O3-Type Cathode for 4.5 V Sodium-Ion Batteries via a Dual-Reductive Coupling Mechanism. *J. Am. Chem. Soc.* **146**, 13924–13933 (2024).
36. Wang, Y. et al. Inverse doping IrO_x/Ti with weakened Ir-O interaction toward stable and efficient acidic oxygen evolution. *Chem* **9**, 2931–2942 (2023).
37. Lee, K. et al. Modulating the valence electronic structure using earth-abundant aluminum for high-performance acidic oxygen evolution reaction. *Chem* **9**, 3600–3612 (2023).
38. Kang, X. et al. A corrosion-resistant RuMoNi catalyst for efficient and long-lasting seawater oxidation and anion exchange membrane electrolyzer. *Nat. Commun.* **14**, 3607 (2023).
39. Luo, Y. et al. Morphology and surface chemistry engineering toward pH-universal catalysts for hydrogen evolution at high current density. *Nat. Commun.* **10**, 269 (2019).
40. Hao, Y. et al. Switching the Oxygen Evolution Mechanism on Atomically Dispersed Ru for Enhanced Acidic Reaction Kinetics. *J. Am. Chem. Soc.* **145**, 23659–23669 (2023).
41. Ge, R. et al. Ultrafine Defective RuO_2 Electrocatayst Integrated on Carbon Cloth for Robust Water Oxidation in Acidic Media. *Adv. Energy Mater.* **9**, 1901313 (2019).
42. Liu, H. et al. Eliminating over-oxidation of ruthenium oxides by niobium for highly stable electrocatalytic oxygen evolution in acidic media. *Joule* **7**, 558–573 (2023).
43. Wang, H.-Y. et al. In Operando Identification of Geometrical-Site-Dependent Water Oxidation Activity of Spinel Co_3O_4. *J. Am. Chem. Soc.* **138**, 36–39 (2016).
44. Guo, L. et al. Phosphorus Defect Mediated Electron Redistribution to Boost Anion Exchange Membrane-Based Alkaline Seawater Electrolysis. *Adv. Energy Mater.* **14**, 2400975 (2024).
45. Lin, C. et al. In-situ reconstructed Ru atom array on α-MnO_2 with enhanced performance for acidic water oxidation. *Nat. Catal.* **4**, 1012–1023 (2021).
46. Wu, H., Huang, Q., Shi, Y., Chang, J. & Lu, S. Electrocatalytic water splitting: Mechanism and electrocatalyst design. *Nano Res* **16**, 9142–9157 (2023).
47. Wang, C. et al. Engineering Lattice Oxygen Activation of Iridium Clusters Stabilized on Amorphous Bimetal Borides Array for Oxygen Evolution Reaction. *Angew. Chem., Int. Ed.* **60**, 27126–27134 (2021).
48. Yao, Y. et al. Engineering the electronic structure of single atom Ru sites via compressive strain boosts acidic water oxidation electrocatalysis. *Nat. Catal.* **2**, 304–313 (2019).
49. Zhang, N. et al. Surface Activation and Ni-S Stabilization in NiO/NiS_2 for Efficient Oxygen Evolution Reaction. *Angew. Chem., Int. Ed.* **61**, e202207217 (2022).
50. Xu, J. et al. $IrO_x \cdot n\,H_2O$ with lattice water–assisted oxygen exchange for high-performance proton exchange membrane water electrolyzers. *Sci. Adv.* **9**, eadh1718 (2023).
51. Xin, S. et al. Coupling Adsorbed Evolution and Lattice Oxygen Mechanism in Fe-$Co(OH)_2$/Fe_2O_3 Heterostructure for Enhanced Electrochemical Water Oxidation. *Adv. Funct. Mater.* **33**, 2305243 (2023).
52. Jiao, S., Fu, X. & Huang, H. Descriptors for the evaluation of electrocatalytic reactions: d-band theory and beyond. *Adv. Funct. Mater.* **32**, 2107651 (2022).
53. Huang, Z.-F. et al. Strategies to break the scaling relation toward enhanced oxygen electrocatalysis. *Matter* **1**, 1494–1518 (2019).
54. Hafner, J. Ab-initio simulations of materials using VASP: Density-functional theory and beyond. *J. Comput. Chem.* **29**, 2044–2078 (2008).
55. Grimme, S. Semiempirical GGA-type density functional constructed with a long-range dispersion correction. *J. Comput. Chem.* **27**, 1787–1799 (2006).
56. Kresse, G. & Joubert, D. From ultrasoft pseudopotentials to the projector augmented-wave method. *Phys. Rev. B* **59**, 1758 (1999).
57. Moellmann, J. & Grimme, S. DFT-D3 study of some molecular crystals. *J. Phys. Chem. C.* **118**, 7615–7621 (2014).
58. Henkelman, G., Arnaldsson, A. & Jónsson, H. A fast and robust algorithm for Bader decomposition of charge density. *Comput. Mater. Sci.* **36**, 354–360 (2006).
59. Peterson, A. A., Abild-Pedersen, F., Studt, F., Rossmeisl, J. & Nørskov, J. K. How copper catalyzes the electroreduction of carbon dioxide into hydrocarbon fuels. *Energy Environ. Sci.* **3**, 1311–1315 (2010).
60. Legrain, F., Carrete, J., van Roekeghem, A., Curtarolo, S. & Mingo, N. How chemical composition alone can predict vibrational free energies and entropies of solids. *Chem. Mater.* **29**, 6220–6227 (2017).

Acknowledgements

This work was partly supported by National Natural Science Foundation of China (No. U24A2079, 51973200, 52202050, and 21905253), Natural Science Foundation of Henan (202300410372), the China Postdoctoral Science Foundation (2022TQ0286) and Joint Fund of Science and Technology R&D Plan of Henan Province (232301420042). We also acknowledge the Center for Modern Analysis and Gene Sequencing of Zhengzhou University and the BL14W beamline of Shanghai Synchrotron Radiation Facility for supporting this project. X.Y. would like acknowledge Leverhulme Trust for financial support. G.I.N.W acknowledge funding support from the Royal Society Te Apārangi (James Cook Research Fellowship), the Ministry of Business Innovation and Employment (C05X2007, UOCX2118), and a philanthropic donation from Greg and Kathryn Trounson.

Author contributions

S.Y.L. and J.W.C. supervised all the aspects of this research. H.W. carried out the experiment, electrocatalytic evaluations, characterizations of the as-prepared electrocatalysts, interpreted the experimental data, and wrote this paper. Z.Z.F., J.K.Y. and X.Y. performed the DFT calculations. H.W., S.Y.W., J.L. and Z.A.H participated in the work and discussed the experimental findings. Z.Y.T., J.B.C. and G.I.N.W revised this manuscript and provided professional suggestions for this work. All the authors participated in commenting on the manuscript.

Competing interests

The authors declare no competing interests.

Additional information

Supplementary information The online version contains supplementary material available at https://doi.org/10.1038/s41467-025-59472-0.

Correspondence and requests for materials should be addressed to Jiangwei Chang or Siyu Lu.

Peer review information *Nature Communications* thanks Gustav Wiberg, Yan Zhao and the other, anonymous, reviewer(s) for their contribution to the peer review of this work. A peer review file is available.